Enhanced Exciton-Exciton Collisions in an Ultraflat Monolayer $MoSe_2$ Prepared through Deterministic Flattening

Takato Hotta[1], Akihiko Ueda[1], Shohei Higuchi[1], Mitsuhiro Okada[2], Tetsuo Shimizu[2], Toshitaka Kubo[2], Keiji Ueno[3], Takashi Taniguchi[4], Kenji Watanabe[5], and Ryo Kitaura[1,*]

[1]*Department of Chemistry, Nagoya University, Nagoya, Aichi 464-8602 Japan*
[2]*Nanomaterials Research Institute, National Institute of Advanced Industrial Science and Technology (AIST), Tsukuba, Ibaraki 305-8565, Japan*
[3]*Department of Chemistry, Saitama University, Saitama 338-8570, Japan*
[4]*International Center for Materials Nanoarchitectonics, National Institute for Materials Science, Tsukuba, Ibaraki 305-0044, Japan*
[5]*Research Center for Functional Materials, National Institute for Materials Science, Tsukuba, Ibaraki 305-0044, Japan*

Corresponding Author: R. Kitaura, r.kitaura@nagoya-u.jp

Abstract

Squeezing bubbles and impurities out of interlayer spaces by applying force through a few-layer graphene capping layer leads to van der Waals heterostructures with the ultraflat structure free from random electrostatic potential arising from charged impurities. Without the graphene capping layer, a squeezing process with an AFM tip induces applied-force-dependent charges of $\Delta n \sim 2 \times 10^{12}$ cm^{-2} μN^{-1}, resulting in the significant intensity of trions in photoluminescence spectra of $MoSe_2$ at low temperature. We found that a hBN/$MoSe_2$/hBN prepared with the "graphene-capping-assisted AFM nano-squeezing method" shows a strong excitonic emission with negligible trion peak, and the residual linewidth of the exciton peak is only 2.2 meV, which is comparable to the homogeneous limit. Furthermore, in this high-quality sample, we found that the formation of biexciton occurs even at extremely low excitation power ($\Phi_{ph} \sim 2.3 \times 10^{19}$ cm^{-2} s^{-1}) due to the enhanced collisions between excitons.

Keywords: two-dimensional materials, van der Waals heterostructures, deterministic flattening, optical physics, microspectroscopy, biexcitons

2D materials, such as graphene and transition metal dichalcogenides (TMDs), have provided fascinating fields for investigating physics in the realm of two-dimensional systems.[1-5] The reduced dimensionality in 2D materials leads to significant many-body effects due to the weakened Coulomb screening and confinement of carriers, resulting in strong excitonic effects in response to optical excitations,[6-9] enhanced charge-density-wave order,[10-13] *etc*. The reduced dimensionality also leads to broken inversion symmetry, which causes the emergence of the valley degree of freedom in, for example, a 2D TMD.[14-17] Moreover, the Fermi level of 2D materials can easily be tuned through applying gate voltage in 2D-material-based field-effect transistors.[18-22] These excellent characteristics of 2D materials enable us to explore a wide range of fundamental physics and possibilities on the realization of the next-generation optoelectronic devices.[3, 23]

For the exploration of the intrinsic properties of 2D materials, the environmental effects need to be suppressed. This is because, in the case of atomically thin materials, environments, including substrates and adsorbates, can drastically alter their optical and electronic properties. For example, substrate-induced roughness causes inhomogeneity in the electronic structure and additional carrier scatterings, leading to inhomogeneous broadening in optical spectra and reduction of carrier mobility in 2D materials.[24-26] Furthermore, substrates sometimes have charged impurities and low-energy phonons, which also contribute to the decrease in carrier mobility. In fact, early works on graphene on SiO_2/Si show mobility ~ $10^4 cm^2/Vs$ even at cryogenic temperature,[27] which is far from the theoretical phonon-limit carrier mobility.[28] Adsorbates also cause inhomogeneous broadening in optical spectra and reduction of carrier mobility in a similar way. Suppression of these unwanted environmental effects thus crucial for investigations of intrinsic properties of 2D materials.

One of the best ways to suppress the environmental effects is encapsulating 2D materials with hexagonal boron nitride (hBN) flakes: hBN/a 2D layer/hBN. hBN is a layered insulator with a large bandgap of ~ 6 eV.[29] The important thing is that hBN has an atomically flat surface without dangling bonds, charged impurities, and low-energy optical phonons. 2D materials encapsulated by hBN flakes, therefore, are free from the environmental effects arising from substrates and adsorbates.[30] For example, in hBN-encapsulated semiconducting TMDs, full width at half maximum (FWHM) of photoluminescence (PL) peaks is much smaller than those of TMDs on SiO_2/Si, reaching the value of the intrinsic limit (neutral exciton of MoS_2: ~ 2 meV at 4 K).[25] Sharp optical responses in hBN-encapsulated structures have led to observations of various intriguing optical responses originating from long-lived interlayer excitons and moiré excitons *etc.*[31-33]

Whereas hBN-encapsulated structures give the ideal platform for 2D materials research, its fabrication process is one of the most severe bottlenecks in the research on 2D materials. The standard fabrication technique is the dry-transfer method based on the pick-up-and-drop process,

where 2D layers are consecutively picked up with the top hBN flake. In this process, bubbles or impurities derived from hydrocarbon are inevitably encapsulated between layers.[34] The bubbles and impurities are sources of inhomogeneity in the electronic structure and carrier scatterings, significantly damaging the quality of hBN-encapsulated structures. Performing the process under vacuum condition or repeated pressing against a substrate[35-37] can reduce bubbles and impurities, but complete removal is still challenging. If we can develop a sure way to fabricate high-quality atomically-flat vdW heterostructures, it should significantly contribute to exploring the fascinating possibilities of 2D materials.

In this work, we have developed a method, the graphene-capping-assisted AFM nano-squeezing (GCAN) method, to fabricate high-quality ultraflat vdW heterostructures to observe their intrinsic properties. Sweeping the sample surface with an AFM tip, the nano-squeezing method,[38, 39] is one of the sure ways to remove impurities and bubbles encapsulated between layers in vdW heterostructure (Fig. 1a). We found, however, that optical responses and electronic transport properties of samples prepared by the nano-squeezing method are strongly influenced by charged impurities: intense PL from trions and saturation of carrier mobility at cryogenic temperature. This result strongly suggests that the nano-squeezing process causes a significant amount of charged impurities on the surface of vdW heterostructures. To suppress the effect from charged impurities, we put a few-layer graphene flake as a capping layer before the squeezing process; the graphene capping layer can effectively screen the unwanted effect from charged impurities (Fig. 1b). PL spectra of the hBN/$MoSe_2$/hBN prepared with the GCAN method gives a very low intensity of trion peak even at cryogenic temperature and a very narrow linewidth approaching the intrinsic limit. Moreover, we found collisions between two excitons occurred even at extremely low excitation power with CW laser (photon flux: $\Phi_{ph} \sim 2.3 \times 10^{19}$ cm^{-2} s^{-1}) in the high-quality sample prepared with the GCAN method.

RESULT AND DISCUSSION

We fabricated hBN/$MoSe_2$/hBN by the standard dry transfer method (see experimental and supplement information). Figure 2a-c shows an optical microscope image of a hBN/$MoSe_2$/hBN sample before and after the nano-squeezing process. As seen in the images, black contrasts arising from encapsulated bubbles and impurities disappear after the nano-squeezing process at 0.8 μN; bubbles and contaminants are removed to be accumulated at the edges of the squeezed area. Residual mean square (RMS) roughness at the squeezed area (Fig. 2c) is only 0.36 nm, clearly showing an atomically flat surface after the squeezing process.

Figure 3a shows PL spectra at 10 K before and after the squeezing. Two sharp peaks at ~ 1.64 eV and ~ 1.61 eV arise from the radiative recombinations of excitons and trions, respectively.[40] In the case of a non-squeezed (dirty) sample, the additional broad peaks at 1.50 eV, which

originates from bound excitons trapped around impurities,[41] are observed. On the other hand, in the case of the squeezed sample, there are no peaks at the low energy region, and the linewidth of exciton emission is reduced from 12 to 4 meV. These results clearly demonstrate that inhomogeneous broadening in PL spectra can be strongly suppressed by the squeezing process, being consistent with the reduction in RMS roughness after the squeezing. The ultraflat structure obtained with the squeezing method is essential to observe sharp optical responses of 2D materials.

Although the squeezing process removes the encapsulated impurities, low-temperature PL spectroscopy shows a significant effect of charged impurities. Figure 3a shows PL spectra of squeezed samples measured at 10 K. As clearly seen, PL spectra significantly change depending on the force applied during the squeezing process; the intensities of low energy peak increase as the force increases. The low-energy peak is assigned to radiative recombinations of trions because of the binding energy of 30 meV,[42] excitation power dependence of peak intensity,[43-45] and gate-voltage dependence of PL spectra[46] (Fig. S2b). Because we used the bottom hBN with a thickness of 20 ~ 40 nm to suppress the substrate-induced potential fluctuation, the observed PL from trions cannot be attributed to the effect from SiO_2/Si substrates. As shown in Fig. 3b, the intensity ratio between the exciton peak and the trion peak (I_{ex}/I_{tr}) shows an exponential decrease against the force applied. A similar exponential decrease in I_{ex}/I_{tr} is also seen in the gate-voltage dependence, and therefore, the observed exponential decrease means that the stronger the force applied during a squeezing process is the more carrier is induced in the encapsulated monolayer $MoSe_2$. Based on the comparison between the force dependence and the gate-voltage dependence, we estimated that the number of tip-induced carriers (Δn) as $\Delta n \sim 2 \times 10^{12}$ cm^{-2} μN^{-1} (details are shown in Fig. S3). Because an AFM tip directly scratches the surface of a top hBN flake during a squeezing process, the process can etch top most hBN surface to induce dangling bonds or cause impurities arising from the AFM tip. These dangling bonds and the tip-induced impurities can be charged impurities sitting adjacent to the encapsulated $MoSe_2$, and the induced charged impurities probably lead to the observed decrease in I_{ex}/I_{tr} shown in Fig. 3b. Note that the tip-induced random electrostatic potential causes not hole doping but electron doping because of the location of the Fermi level in $MoSe_2$; the Fermi level locates at an energy close to the conduction band minimum and the valence band maximum is far away from the Fermi level.

To confirm the existence of charged impurity after a squeezing process, we measured a temperature dependence in carrier mobility of a hBN/graphene/hBN sample, which was prepared through the standard pick-up-and-drop method and the squeeze method with an applied force of 1.8 μN. Figure 3c represents a temperature dependence of electron and hole mobility, μ_e and μ_h, determined from Hall measurements performed in the temperature range of 4.5 to 300 K (Fig. S4). As shown in Fig. 3c, μ_e and μ_h increase as temperature decreases. In the high-temperature region, the observed relation between mobilities and temperature is close to μ_e (μ_h) $\propto T^{-1}$, which

is consistent with acoustic phonon scattering in two-dimensional electronic systems.[28] In contrast, the increase in mobilities deviates from the relation, μ_e (μ_h) $\propto T^{-1}$, as temperature decrease and saturates below 80 K to be ~ 2.7 × 10^4 (μ_e) and 2.2 × 10^4 (μ_h) $cm^2 V^{-1} s^{-1}$. The surface roughness of this sample is small enough (RMS roughness is 0.18 nm) after the squeezing process, and the roughness scattering in this sample should be strongly suppressed. The observed leveling off in carrier mobilities at around 2~3 × 10^4 (μ_h) $cm^2 V^{-1} s^{-1}$ thus should arise from charged impurities scattering,[47] being consistent with the results of PL spectroscopy obtained with a hBN-encapsulated monolayer $MoSe_2$. Dirac points in output curves of the hBN/graphene/hBN (Fig. S4d) does not locate at zero, indicating that carriers are induced in response to charges induced on the top of hBN after the process.

To further confirm if charged impurities can be induced by squeezing processes or not, electrostatic force microscope (EFM) observations were performed. Figure 4b-d show EFM images and the corresponding line profiles of a hBN/hBN flake (Fig. 4a) before and after a nano-squeezing process. As clearly seen in these images, the electrostatic potential at the hBN surface significantly changes after the squeezing process (an increase from 0.5 to 0.7 mV). Note that the morphology and height of the hBN flake remain intact after the squeezing process, and the observed change in electrostatic potential should be caused by the change in surface properties. The increase in electrostatic potential, therefore, strongly indicates that squeezing processes can induce charges on the surface of the top hBN, being consistent with the results on PL and transport properties of samples prepared with the nano-squeezing method.

To suppress the effect of induced charged impurities, we put a few-layer graphene flake on top of a hBN/$MoSe_2$/hBN before a squeezing process. In the GCAN method, the graphene capping layer can effectively screen Coulomb interaction from the charged impurities induced on the topmost surface, thereby leading to ultraflat monolayer $MoSe_2$ free from the effect of charged impurities.[48, 49] Figure 5a shows an optical microscope image of the hBN/$MoSe_2$/hBN sample with few-layer graphene capping layer, where a bottom graphene layer was additionally put under the hBN-encapsulated $MoSe_2$ to screen Coulomb interaction from charged impurity in the underlying SiO_2/Si substrate; the region surrounded by the red box in the image was squeezed with an applied force of 1.5 μN (Fig. 5b). As shown in Fig. 5c, the PL spectrum measured at 10 K clearly shows very low intensity of the low-energy peak at 1.61 eV, meaning that the few-layer graphene capping layer successfully screens Coulomb potential arising from the charged impurities; the very low intensity also means minimal unintentional doping into the encapsulated monolayer $MoSe_2$. Note that even without the graphene bottom layer, the hBN/$MoSe_2$/hBN sample prepared by the GCAN method shows a single PL peak without the contribution from trions, which means that the GCAN method alone can significantly suppress the extrinsic potential fluctuation (Fig. S5). In this sample, both the top and bottom graphene layers do not

touch the $MoSe_2$ directly, and neither neutralization nor the fast non-radiative energy transfer, which contributes to quench PL from trions, are expected. The residual linewidth of exciton emission determined through a least-square fitting with Voigt function is small, 2.2 meV (Fig. S6), which is comparable to the intrinsic PL linewidth reported.[25, 50, 51]

Reflecting the high quality of the sample prepared with the GCAN method, efficient exciton-exciton collisions were observed. Figure 6a shows an excitation power dependence of PL spectra measured with a 633 nm continuous wave (CW) laser. As clearly seen, a peak, whose intensity drastically increases as excitation laser power increases, emerges at ~ 1.62 eV in addition to the excitonic peak at ~ 1.645 eV; the low-energy peak is denoted by X′. To address the origin of X′, we plotted I_{ex} and intensities of X′ with respect to photon flux (Φ_{ph}). As shown in Fig. 6b, while I_{ex} is proportional to Φ_{ph} as expected, intensities of X′ are proportional to Φ_{ph},[1.8] which strongly suggest that X′ originates from an excited state formed through two-body collisions of excitons (see also Fig. S7 and S8). There are two possible origins for the excited state, biexcitons,[41, 44, 51-53] and trions. Binding energy alone is insufficient to unambiguously assign X′ because of the small difference in binding energy between biexcitons and trions in $MoSe_2$: trion: 27.7 ~ 31 meV and biexciton: 17.7 ~ 23 meV.[42, 50, 61-64] To address the origin of X′, we investigated excitation-power dependence on peak position of X′ (Fig. S9). If X′ arises from trions, photo-induced carriers, which are generated through exciton-exciton annihilation processes, should exist, and the number of the photo-induced carriers should increase as Φ_{ph} increases. In this case, the position of X′ should show an energy shift to the red side due to the increase of quasi-Fermi level.[64] As clearly seen in Fig. S9, this is totally inconsistent with the observed blue shift, suggesting X′ originates from biexcitons. Moreover, CCD images of PL spectra measured with different Φ_{ph} (Fig. S10) show no enhancement in diffusion, which enhancement is expected due to the formation of hot excitons through exciton-exciton annihilations. We, therefore, conclude that X′ can be assigned as biexciton emission. Note that this peak does not originate from the formation of excited states of excitons (2s or 3s state),[7, 51] which is another possible process when two excitons collide, because the energy difference between the low-energy peak and the exciton peak is less than that of the excited states and the ground state.

In the sample prepared with the GCAN method, exciton-exciton collision is greatly enhanced. As seen in Fig. 6a, the generation of biexcitons occurs even at small Φ_{ph} of 2.3×10^{19} cm^{-2} s^{-1} whereas the biexciton formation has not been seen in samples prepared without a graphene capping layer even with much higher Φ_{ph} of 5.1×10^{21} cm^{-2} s^{-1} and even with pulsed excitations (pulse duration ~ 60 ps) with photon density of 5.1×10^{14} cm^{-2} per pulse (Fig. S2b). To make sure the generation of biexcitons is reasonable, we compared average exciton-exciton distance d_{ex} with exciton diffusion length L_{ex}. The d_{ex} can be calculated as $d_{ex} = 1/\sqrt{\alpha \cdot \tau_{ex} \cdot \Phi_{ph}}$, where α and τ_{ex} represent absorptance and exciton lifetime, respectively. Using values of $\alpha = 0.07$,[33]

τ_{ex} = 47 ps and Φ_{ph} = 2.3 × 10^{19} cm^{-2} s^{-1}, we obtained d_{ex} = 1.1 μm; lifetime of excitons is measured with time-correlated single-photon counting (TSCPC) method (Fig. S11). The L_{ex} can be calculated with the following equation, $L_{ex} = 2\sqrt{D_{ex}\tau_{ex}}$, where D_{ex} is the diffusion coefficient. The D_{ex} is determined with the Einstein relation, $D_{ex} \sim k_B T / M_{ex}\gamma$, where k_B, M_{ex}, and γ correspond to Boltzmann's constant, exciton translational mass (~ 0.3 m_0)[54] and homogeneous linewidth of exciton emission (half-width at half-maximum of Lorentzian linewidth obtained through a least-square fitting with Voigt function).[55] In this case, the γ is only 0.5 meV at 10 K, corresponding to a momentum relaxation time of 2.3 ps (Fig. S12). Using the determined value of D_{ex}, 11 cm^2 s^{-1}, the L_{ex} is calculated as 0.5 μm, being comparable with the d_{ex} calculated with the smallest Φ_{ph} used in this experiment. This indicates that diffusion alone can cause inter-exciton collisions to form biexcitons in the present high-quality sample. In addition, inter-exciton attractive interactions, such as phonon-mediated effective interaction,[59, 60] may drive drift of excitons, enhancing inter-exciton collisions in the high-quality sample.

Previous papers report that hBN substrates reduce the exciton-exciton annihilation (EEA) rate compared to SiO_2/Si substrates.[65] In the case of TMDs in touch with a SiO_2 substrate, the potential fluctuation, which originates from the SiO_2 substrate, probably causes the shallow trappings for excitons generated in TMDs. Under this situation, the density of excitons can be locally large due to the trappings, and this may lead to EEA rate constants that are larger than those of hBN/TMD/hBN. In contrast, in the case of hBN/TMD/hBN, the hBN encapsulation significantly suppress the formation of shallow trappings for excitons, and we can observe the intrinsic diffusion of excitons in this case. In addition to the hBN-encapsulation, the GCAN method can further reduce extrinsic effects arising from bubbles and impurities, leading to high-mobility excitons. As a result of the intrinsic diffusion with high mobility, exciton-exciton collisions can occur even at a small photon flux of 2.3 × 10^{19} cm^{-2} s^{-1} in our high-quality sample. Monte Carlo simulation on exciton-exciton collisions shows that the longer the diffusion length is, the higher the probability of collision becomes, which supports our experimental observations (Fig. S13).

CONCLUSION

In conclusion, we have successfully developed a sample preparation technique, the GCAN method, to surely fabricate high-quality vdW heterostructures. The key idea in this technique is squeezing bubbles and impurities through a few-layer graphene capping layer to have ultraflat heterostructures free from random electrostatic potential arising from charged impurities. Without a graphene capping layer, a sweeping with an AFM tip induces applied-force-dependent charges of Δn ~ 2 × 10^{12} cm^{-2} μN^{-1}, leading to strong PL intensity of trions and level off of carrier mobility at low temperature. A hBN/$MoSe_2$/hBN prepared with the GCAN method shows a strong excitonic emission with a negligible trion peak, and the residual linewidth of the excitonic peak

is only 2.2 meV. Furthermore, in this high-quality sample, we found that biexciton formation occurs even at very low excitation power (Φ_{ph} ~ 2.3 × 10^{19} cm^{-2} s^{-1}) due to the enhanced collisions between excitons arising from long exciton diffusion length. This work has established a avenue for exploring the physics of 2D materials based on ultraflat vdW heterostructures free from random electrostatic potential.

EXPERIMENTAL METHODS

Fabrication of vdW heterostructures. Monolayer $MoSe_2$, graphene, and hBN flakes used to fabricate vdW heterostructures were mechanically exfoliated from bulk crystals and deposited onto SiO_2/Si substrates. Firstly, a hBN flake was picked up with a polymer stamp,[56, 57] and then other flakes were consecutively picked up with the hBN flake on the polymer stamp. Note that we heated substrates to 110 ~ 130 ºC to make contact between flakes better during pick-up processes. Finally, the polymer stamp with vdW heterostructure on top was transferred onto another hBN flake on a SiO_2/Si substrate. Polymer on the vdW heterostructure was removed by soaking in chloroform overnight. In the case of a sample with a graphene capping layer, instead of a hBN flake, a few-layer graphene flake was picked up first, and other flakes were consecutively picked up. To remove bubbles and impurities encapsulated between layers, we applied force by sweeping the surface of samples with an AFM-tip working under contact mode (BRUKER Inc., Dimension FastScan). Before sweeping the sample surface, the applied force was calibrated by the bare surface of SiO_2/Si substrates using the torsional Sader method.[58] Typical scan lines and scan rate in the sweeping processes were 512 – 2024 lines and 0.8 – 1 Hz, respectively.

Electrostatic force microscopy (EFM) measurement. EFM images were obtained with a commercial AFM setup (Park SYSTEMS, NX10 EFM operating at EFM mode) and a conductive AFM cantilever (Olympus, OMCL-AC240TM Pt coated). We made electrical contact between substrates and the sample stage by Ag paste. All EFM images were taken under the following experimental conditions: 512 lines, 25×25 μm^2, Scan rate: 0.3 – 0.05 Hz, sample bias voltage: 0 V and dark environment.

Optical measurements. Optical responses were obtained with a home-made microspectroscopy system. We used a HeNe CW laser (Thorlabs, HNL050L) and a pulsed super-continuum white laser (SuperK EXTREME, NKT Photonic, 40 MHz) for sample excitations. The super-continuum laser was monochromated by a spectrometer (Princeton Instruments, SP2150) to obtain the desired wavelength. The laser beam was focused on a sample by a ×50 objective lens with a correction ring (Nikon, CFI L Plan EPI CR, NA = 0.7). Samples were set on a sample stage cooled

by flowing He liquid under vacuuming (KONTI-Cryostat-Micro, CryoVac), and the sample temperature was monitored and controlled by a temperature controller (TIC 304-MA, CryoVac). The PL signal extracted by a long pass filter (Thorlabs, FELH series) was introduced to a spectrometer (IsoPlane 320, Princeton Instruments) and detected by a charge-coupled device (PIXIS 1024B_eXcelon, Princeton Instruments). We measured time-resolved PL (TRPL) by time-correlated single-photon counting (TCSPC) method with an avalanche photodetector (Becker & Hickl GmbH, ID-100-50-ULN). The obtained data were fitted by double exponential decay function ($I(t) = \mathrm{a}_1 \exp(-t/\tau_1) + (1 - \mathrm{a}_1)\exp(-t/\tau_2)$), where τ_1, τ_2, and a_1 are radiative lifetimes and a fitting parameter.

ASSOCIATED CONTENT

Supporting Information

The Supporting Information is available free of charge.

Optical and AFM images of hBN/$MoSe_2$/hBN heterostructures, PL spectra of the hBN/$MoSe_2$/hBN heterostructure squeezed at 1.5 μN measured at 10 K, Comparing to electrical and tip-induced carrier doping, A graphene Hall bar, The effect of the graphene bottom layer on the PL spectra of $MoSe_2$, Estimation of residual linewidth at 0 K, A log-log plot between integrated peak areas of exciton and the low-energy peak, Excitation power dependence of PL spectra excited with a pulsed laser, Photon flux dependence of peak positions, CCD images of PL spectra, Radiative lifetime of excitons measured by TCSPC method, Extracting homogeneous linewidth by Voigt function, Monte Carlo simulation of exciton-exciton collisions.

Notes

The authors declare no competing financial interest.

ACKNOWLEDGMENTS

R. K. was supported by JSPS KAKENHI Grant numbers JP16H03825, JP16H00963, JP15K13283, JP25107002, and JST CREST Grant Number JPMJCR16F3. T. H. was supported by JSPS KAKENHI Grant number JP19J15359. M. O. was supported by JSPS KAKENHI Grant number JP19K15403. K.W. and T.T. acknowledge support from the Elemental Strategy Initiative conducted by the MEXT, Japan, Grant Number JPMXP0112101001, JSPS KAKENHI Grant Numbers JP20H00354 and the CREST(JPMJCR15F3), JST.

REFERENCES

(1) Manzeli, S.; Ovchinnikov, D.; Pasquier, D.; Yazyev, O. V.; Kis, A. 2D Transition Metal Dichalcogenides. *Nat. Rev. Mater.* **2017**, *2*, 17033.

(2) Wang, Q. H.; Kalantar-Zadeh, K.; Kis, A.; Coleman, J. N.; Strano, M. S. Electronics and Optoelectronics of Two-Dimensional Transition Metal Dichalcogenides. *Nat. Nanotechnol.* **2012**, *7*, 699—712.

(3) Mak, K. F.; Shan, J. Photonics and Optoelectronics of 2D Semiconductor Transition Metal Dichalcogenides. *Nat. Photonics* **2016**, *10*, 216—226.

(4) Xu, M. S.; Liang, T.; Shi, M. M.; Chen, H. Z. Graphene-Like Two-Dimensional Materials. *Chem. Rev.* **2013**, *113*, 3766—3798.

(5) Schaibley, J. R.; Yu, H. Y.; Clark, G.; Rivera, P.; Ross, J. S.; Seyler, K. L.; Yao, W.; Xu, X. D. Valleytronics in 2D Materials. *Nat. Rev. Mater.* **2016,** *1*, 16055.

(6) Mak, K. F.; Lee, C.; Hone, J.; Shan, J.; Heinz, T. F. Atomically Thin MoS_2: A New Direct-Gap Semiconductor. *Phys. Rev. Lett.* **2010**, *105*, 136805.

(7) Han, B.; Robert, C.; Courtade, E.; Manca, M.; Shree, S.; Amand, T.; Renucci, P.; Taniguchi, T.; Watanabe, K.; Marie, X.; Golub, L. E.; Glazov, M. M.; Urbaszek, B. Exciton States in Monolayer $MoSe_2$ and $MoTe_2$ Probed by Upconversion Spectroscopy. *Phys. Rev. X* **2018**, *8*, 031073 .

(8) Morozov, Y. V.; Kuno, M. Optical Constants and Dynamic Conductivities of Single Layer MoS_2, $MoSe_2$, and WSe_2. *Appl. Phys. Lett.* **2015**, *107*, 083103.

(9) Raja, A.; Chaves, A.; Yu, J.; Arefe, G.; Hill, H. M.; Rigosi, A. F.; Berkelbach, T. C.; Nagler, P.; Schuller, C.; Korn, T.; Nuckolls, C.; Hone, J.; Brus, L. E.; Heinz, T. F.; Reichman, D. R.; Chernikov, A. Coulomb Engineering of the Bandgap and Excitons in Two-Dimensional Materials. *Nat. Commun.* **2017**, *8*, 15251.

(10) Bawden, L.; Cooil, S. P.; Mazzola, F.; Riley, J. M.; Collins-McIntyre, L. J.; Sunko, V.; Hunvik, K. W. B.; Leandersson, M.; Polley, C. M.; Balasubramanian, T.; Kim, T. K.; Hoesch, M.; Wells, J. W.; Balakrishnan, G.; Bahramy, M. S.; King, P. D. C. Spin-Valley Locking in the Normal State of a Transition-Metal Dichalcogenide Superconductor. *Nat. Commun.* **2016**, *7*, 11711.

(11) Li, A. J.; Zhu, X. C.; Rhodes, D.; Samouce, C. C.; Balicas, L.; Hebard, A. F. van der Waals Schottky Barriers as Interface Probes of the Correlation between Chemical Potential Shifts and Charge Density Wave Formation in 1T-$TiSe_2$ and 2H-$NbSe_2$. *Phys. Rev. B* **2017,** *96*, 125301.

(12) Miao, G. Y.; Xue, S. W.; Li, B.; Lin, Z. J.; Liu, B.; Zhu, X. T.; Wang, W. H.; Guo, J. D. Real-Space Investigation of the Charge Density Wave in VTe_2 Monolayer with Broken Rotational and Mirror Symmetries. *Phys. Rev. B* **2020**, *101*, 035407.

(13) Sayers, C. J.; Farrar, L. S.; Bending, S. J.; Cattelan, M.; Jones, A. J. H.; Fox, N. A.; Kociok-Kohn, G.; Koshmak, K.; Laverock, J.; Pasquali, L.; Da Como, E. Correlation between Crystal Purity and the Charge Density Wave in 1T-VSe_2. *Phys. Rev. Mater.* **2020**, *4*, 025002.

(14) Onga, M.; Zhang, Y. J.; Ideue, T.; Iwasa Y. Exciton Hall Effect in Monolayer MoS_2. *Nat. Mater.* **2017,**

16, 1193—1197.

(15) Tang, Y. H.; Mak, K. F.; Shan, J. Long Valley Lifetime of Dark Excitons in Single-Layer WSe_2. *Nat. Commun.* **2019**, *10*, 4047.

(16) Xiao, D.; Liu, G. B.; Feng, W. X.; Xu, X. D.; Yao, W. Coupled Spin and Valley Physics in Monolayers of MoS_2 and Other Group-VI Dichalcogenides. *Phys. Rev. Lett.* **2012**, *108*, 196802.

(17) Xu, X. D.; Yao, W.; Xiao, D.; Heinz, T. F. Spin and Pseudospins in Layered Transition Metal Dichalcogenides. *Nat. Phys.* **2014**, *10*, 343—350.

(18) Radisavljevic, B.; Radenovic, A.; Brivio, J.; Giacometti, V.; Kis, A. Singel-Layer MoS_2 Transistors. Nat. Nanotech. **2011**, *6*, 147—150.

(19) Das, S.; Appenzeller, J. WSe_2 Field Effect Transistors with Enhanced Ambipolar Characteristics. *Appl. Phys. Lett.* **2013**, *103*, 103501.

(20) Kanazawa, T.; Amemiya, T.; Ishikawa, A.; Upadhyaya, V.; Tsuruta, K.; Tanaka, T.; Miyamoto, Y. Few-Layer HfS_2 Transistors. *Sci. Rep.* **2016**, *6*, 22277.

(21) Desai, S. B.; Madhvapathy, S. R.; Sachid, A. B.; Llinas, J. P.; Wang, Q. X.; Ahn, G. H.; Pitner, G.; Kim, M. J.; Bokor, J.; Hu, C. M.; Wong, H. S. P.; Javey, A. MoS_2 Transistors with 1-Nanometer Gate Lengths. *Science* **2016**, *354*, 99—102.

(22) Lee, G. H.; Cui, X.; Kim, Y. D.; Arefe, G.; Zhang, X.; Lee, C. H.; Ye, F.; Watanabe, K.; Taniguchi, T.; Kim, P.; Hone, J. Highly Stable, Dual-Gated MoS_2 Transistors Encapsulated by Hexagonal Boron Nitride with Gate-Controllable Contact, Resistance, and Threshold Voltage. *ACS Nano* **2015**, *9*, 7019—7026.

(23) Baugher, B. W. H.; Churchill, H. O. H.; Yang, Y. F.; Jarillo-Herrero, P. Optoelectronic Devices Based on Electrically Tunable *p-n* Diodes in a Monolayer Dichalcogenide. *Nat. Nanotechnol.* **2014**, *9*, 262—267.

(24) Ajayi, O. A.; Ardelean, J. V.; Shepard, G. D.; Wang, J.; Antony, A.; Taniguchi, T.; Watanabe, K.; Heinz, T. F.; Strauf, S.; Zhu, X. Y.; Hone, J. C. Approaching the Intrinsic Photoluminescence Linewidth in Transition Metal Dichalcogenide Monolayers. *2D Mater.* **2017**, *4*, 031011.

(25) Cadiz, F.; Courtade, E.; Robert, C.; Wang, G.; Shen, Y.; Cai, H.; Taniguchi, T.; Watanabe, K.; Carrere, H.; Lagarde, D.; Manca, M.; Amand, T.; Renucci, P.; Tognay, S.; Marie, X.; Urbaszek, B. Excitonic Linewidth Approaching the Homogeneous Limit in MoS_2-Based van der Waals Heterostructures. *Phys. Rev. X* **2017**, *7*, 021026.

(26) Chen, J. H.; Jang, C.; Xiao, S. D.; Ishigami, M.; Fuhrer, M. S. Intrinsic and Extrinsic Performance Limits of Graphene Devices on SiO_2. *Nat. Nanotech.* **2008**, *3*, 206—209.

(27) Zhang, Y. B.; Tan, Y. W.; Stormer, H. L.; Kim, P. Experimental Observation of the Quantum Hall Effect and Berry's Phase in Graphene. *Nature* **2005**, *438*, 201—204.

(28) Hwang, E. H.; Das Sarma, S. Acoustic Phonon Scattering Limited Carrier Mobility in Two-Dimensional Extrinsic Graphene. *Phys. Rev. B* **2008**, *77*, 115449.

(29) Cassabois, G.; Valvin, P.; Gil, B. Hexagonal Boron Nitride is an Indirect Bandgap Semiconductor.

Nat. Photonics **2016**, *10*, 262.

(30) Cui, X.; Lee, G.-H.; Kim, Y. D.; Arefe, G.; Huang, P. H.; Lee, C.-H.; Chenet, D. A.; Zhang, X.; Wang, L.; Ye, F.; Pizzocchero, F.; Jessen, B. S.; Watanabe, K.; Taniguchi, T.; Muller, D. A.; Low, T.; Kim, P.; Hone, J. Multi-Terminal Transport Measurements of MoS_2 Using a van der Waals Heterostructure Device Platform. *Nat. Nanotech.* **2015**, *10*, 534—540.

(31) Seyler, K. L.; Rivera, P.; Yu, H. Y.; Wilson, N. P.; Ray, E. L.; Mandrus, D. G.; Yan, J. Q.; Yao, W.; Xu, X. D. Signatures of Moire-Trapped Valley Excitons in $MoSe_2/WSe_2$ Heterobilayers. *Nature* **2019**, *567*, 66.

(32) Tran, K.; Moody, G.; Wu, F. C.; Lu, X. B.; Choi, J.; Kim, K.; Rai, A.; Sanchez, D. A.; Quan, J. M.; Singh, A.; Embley, J.; Zepeda, A.; Campbell, M.; Autry, T.; Taniguchi, T.; Watanabe, K.; Lu, N.; Banerjee, S. K.; Silveman, K. L.; Kim, S.; *et al*. Evidence for Moire Excitons in van der Waals Heterostructures. *Nature* **2019**, *567*, 71.

(33) Wang, J.; Ardelean, J.; Bai, Y. S.; Steinhoff, A.; Florian, M.; Jahnke, F.; Xu, X. D.; Kira, M.; Hone, J.; Zhu, X. Y. Optical Generation of High Carrier Densities in 2D Semiconductor Heterobilayers. *Sci. Adv.* **2019**, *5*, 0145.

(34) Kretinin, A. V.; Cao, Y.; Tu, J. S.; Yu, G. L.; Jalil, R.; Novoselov, K. S.; Haigh, S. J.; Gholinia, A.; Mishchenko, A.; Lozada, M.; Georgiou, T.; Woods, C. R.; Withers, F.; Blake, P.; Eda, G.; Wirsig, A.; Hucho, C.; Watanabe, K.; Taniguchi, T.; Geim, A. K.; *et al*. Electronic Properties of Graphene Encapsulated with Different Two-Dimensional Atomic Crystals. *Nano Lett.* **2014**, *14*, 3270—3276.

(35) Kang, K.; Lee, K.-H.; Han, Y.; Gao, H.; Xie, S.; Muller, D. A.; Park, J. Layer-by-Layer Assembly of Two-Dimensional Materials into Wafer-Scale Heterostructures. *Nature* **2017**, *550*, 229—233.

(36) Purdie, D. G.; Pugno, N. M.; Taniguchi, T.; Watanabe, K.; Ferrari, A. C.; Lombardo, A. Cleaning Interfaces in Layered Materials Heterostructures. *Nat. Commun.* **2018**, *9,* 5387.

(37) Lu, X. B.; Stepanov, P.; Yang, W.; Xie, M.; Aamir, M. A.; Das, I.; Urgell, C.; Watanabe, K.; Taniguchi, T.; Zhang, G. Y.; Bachtold, A.; MacDonald, A. H.; Efetov, D. K. Superconductors, Orbital Magnets and Correlated States in Magic-Angle Bilayer Graphene. *Nature* **2019**, *574*, 653.

(38) Rosenberger, M. R.; Chuang, H. J.; McCreary, K. M.; Hanbicki, A. T.; Sivaram, S. V.; Jonker, B. T. Nano-"Squeegee" for the Creation of Clean 2D Material Interfaces. *ACS Appl. Mater. Interfaces* **2018**, *10*, 10379—10387.

(39) Hanbicki, A. T.; Chuang, H. J.; Rosenberger, M. R.; Hellberg, C. S.; Sivaram, S. V.; McCreary, K. M.; Mazin, II; Jonker, B. T. Double Indirect Interlayer Exciton in a $MoSe_2/WSe_2$ van der Waals Heterostructure. *ACS Nano* **2018**, *12*, 4719—4726.

(40) Arora, A.; Nogajewski, K.; Molas, M.; Koperski, M.; Potemski, M. Exciton Band Structure in Layered $MoSe_2$: From a Monolayer to the Bulk Limit. *Nanoscale* **2015**, *7*, 20769—20775.

(41) Tongay, S.; Suh, J.; Ataca, C.; Fan, W.; Luce, A.; Kang, J. S.; Liu, J.; Ko, C.; Raghunathanan, R.; Zhou, J.; Ogletree, F.; Li, J.; Grossman, J. C.; Wu, J. Defects Activated Photoluminescence in Two-

Dimensional Semiconductors: Interplay between Bound, Charged, and Free Excitons. *Sci. Rep.* **2013**, *3*, 2657.

(42) Hao, K.; Specht, J. F.; Nagler, P.; Xu, L. X.; Tran, K.; Singh, A.; Dass, C. K.; Schuller, C.; Korn, T.; Richter, M.; Knorr, A.; Li, X.; Moody, G. Neutral and Charged Inter-Valley Biexcitons in Monolayer $MoSe_2$. *Nat. Commun.* **2017**, *8,* 15552.

(43) Vaclavkova, D.; Wyzula, J.; Nogajewski, K.; Bartos, M.; Slobodeniuk, A. O.; Faugeras, C.; Potemski, M.; Molas, M. R. Singlet and Triplet Trions in WS_2 Monolayer Encapsulated in Hexagonal Boron Nitride. *Nanotechnology* **2018**, *29*, 32.

(44) Okada, M.; Miyauchi, Y.; Matsuda, K.; Taniguchi, T.; Watanabe, K.; Shinohara, H.; Kitaura, R. Observation of Biexcitonic Emission at Extremely Low Power Density in Tungsten Disulfide Atomic Layers Grown on Hexagonal Boron Nitride. *Sci. Rep.* **2017**, *7*, 322.

(45) Huang, J. N.; Hoang, T. B.; Mikkelsen, M. H. Probing the Origin of Excitonic States in Monolayer WSe_2. *Sci. Rep.* **2016**, *6*, 22414.

(46) Shepard, G. D.; Ardelean, J. V.; Ajayi, O. A.; Rhodes, D.; Zhu, X. Y.; Hone, J. C.; Strauf, S. Trion-Species-Resolved Quantum Beats in $MoSe_2$. *ACS Nano* **2017**, *11*, 11550—11558.

(47) Srivastava, P. K.; Ghosh, S. Defect Engineering as a Versatile Route to Estimate Various Scattering Mechanisms in Monolayer Graphene on Solid Substrates. *Nanoscale* **2015**, *7*, 16079—16086.

(48) Maher, P.; Wang, L.; Gao, Y. D.; Forsythe, C.; Taniguchi, T.; Watanabe, K.; Abanin, D.; Papic, Z.; Cadden-Zimansky, P.; Hone, J.; Kim, P.; Dean, C. R. Tunable Fractional Quantum Hall Phases in Bilayer Graphene. *Science* **2014**, *345*, 61—64.

(49) Uwanno, T.; Taniguchi, T.; Watanabe, K.; Nagashio, K. Electrically Inert h-BN/Bilayer Graphene Interface in All-Two-Dimensional Heterostructure Field Effect Transistors. *ACS Appl. Mater. Interfaces* **2018**, *10*, 28780—28788.

(50) Shree, S.; Semina, M.; Robert, C.; Han, B.; Amand, T.; Balocchi, A.; Manca, M.; Courtade, E.; Marie, X.; Taniguchi, T.; Watanabe, K.; Glazov, M. M.; Urbaszek, B. Observation of Exciton-Phonon Coupling in $MoSe_2$ Monolayers. *Phys. Rev. B* **2018**, *98*, 035302.

(51) Lorchat, E.; Lopez, L. E. P.; Robert, C.; Lagarde, D.; Froehlicher, G.; Taniguchi, T.; Watanabe, K.; Marie, X.; Berciaud, S. Filtering the Photoluminescence Spectra of Atomically Thin Semiconductors with Graphene. *Nat. Nanotech.* **2020**, *15*, 283.

(52) He, Z. Y.; Xu, W. S.; Zhou, Y. Q.; Wang, X. C.; Sheng, Y. W.; Rong, Y. M.; Guo, S. Q.; Zhang, J. Y.; Smith, J. M.; Warner, J. H. Biexciton Formation in Bilayer Tungsten Disulfide. *ACS Nano* **2016**, *10*, 2176—2183.

(53) Paradisanos, I.; Germanis, S.; Pelekanos, N. T.; Fotakis, C.; Kymakis, E.; Kioseoglou, G.; Stratakis, E. Room Temperature Observation of Biexcitons in Exfoliated WS_2 Monolayers. *Appl. Phys. Lett.* **2017**, *110*, 193102.

(54) Goryca, M.; Li, J.; Stier, A. V.; Taniguchi, T.; Watanabe, K.; Courtade, E.; Shree, S.; Robert, C.;

Urbaszek, B.; Marie, X.; Crooker, S. A. Revealing Exciton Masses and Dielectric Properties of Monolayer Semiconductors with High Magnetic Fields. *Nat. Commun.* **2019**, *10*, 4172.

(55) Moody, G.; Dass, C. K.; Hao, K.; Chen, C. H.; Li, L. J.; Singh, A.; Tran, K.; Clark, G.; Xu, X. D.; Berghauser, G.; Malic, E.; Knorr, A.; Li, X. Intrinsic Homogeneous Linewidth and Broadening Mechanisms of Excitons in Monolayer Transition Metal Dichalcogenides. *Nat. Commun.* **2015**, *6*, 8315.

(56) Masubuchi, S.; Morimoto, M.; Morikawa, S.; Onodera, M.; Asakawa, Y.; Watanabe, K.; Taniguchi, T.; Machida, T. Autonomous Robotic Searching and Assembly of Two-Dimensional Crystals to Build van der Waals Superlattices. *Nat. Commun.* **2018**, *9*, 1413.

(57) Uchiyama, Y.; Kutana, A.; Watanabe, K.; Taniguchi, T.; Kojima, K.; Endo, T.; Miyata, Y.; Shinohara, H.; Kitaura, R. Momentum-Forbidden Dark Excitons in hBN-Encapsulated Monolayer MoS_2. *npj 2D Mater. Appl.* **2019**, *3*, 1—6.

(58) Sader, J. E.; Chon, J. W. M.; Mulvaney, P. Calibration of Rectangular Atomic Force Microscope Cantilevers. *Rev. Sci. Instrum.* **1999,** *70*, 3967—3969.

(59) Schmit, P. P. The Interaction between Mott-Wannier Excitons in a Vibrating Lattice. *J. Phys. C: Sol. Stat. Phys.* **1969,** *2*, 785.

(60) Shahnazaryan, V.; Shelykh, I. A.; Kyriienko, O. Attractive Coulomb Interaction of Two-Dimensional Rydberg Excitons. *Phys. Rev. B* **2016**, *93*, 9.

(61) Kylanpaa, I.; Komsa, H. P. Binding Energies of Exciton Complexes in Transition Metal Dichalcogenide Monolayers and Effect of Dielectric Environment. *Phys. Rev. B* **2015,** *92*, 6.

(62) Szyniszewski, M.; Mostaani, E.; Drummond, N. D.; Fal'ko, V. I. Binding Energies of Trions and Biexcitons in Two-Dimensional Semiconductors from Diffusion Quantum Monte Carlo Calculations. *Phys. Rev. B* **2017,** *95*, 5.

(63) Zhang, D. K.; Kidd, D. W.; Varga, K. Excited Biexcitons in Transition Metal Dichalcogenides. *Nano Lett.* **2015,** *15*, 7002—7005.

(64) Roch, J. G.; Leisgang, N.; Froehlicher, G.; Makk, P.; Watanabe, K.; Taniguchi, T.; Schonenberger, C.; Warburton, R. J. Quantum-Confined Stark Effect in a MoS_2 Monolayer van der Waals Heterostructure. *Nano Lett.* **2018,** *18*, 1070—1074.

(65) Hoshi, Y; Kuroda, T.; Okada, M.; Moriya, S.; Masubuchi, S.; Watanabe, K.; Taniguchi, T.; Kitaura, R.; Machida, T. Suppression of Exciton-Exciton Annihilation in Tungsten Disulfide Monolayers Encapsulated by Hexagonal Boron Nitrides. *Phys. Rev. B* **2018,** *95*, 241403.

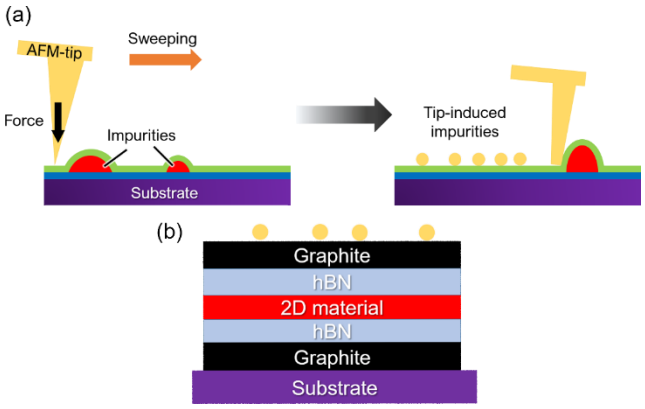

Figure 1 (a) A schematic image showing the nano-squeezing process by an AFM tip sweeping. Impurities encapsulated between layers can be squeezed out, but sweeping-induced impurities attach to the surface. (b) A schematic image of a hBN-encapsulated 2D material with a few-layer graphene capping layer, which can screen random Coulomb potential arising from the sweeping-induced impurities. A graphite bottom layer is also put to screen Coulomb potential arising from charged impurities locate at the underlying SiO_2/Si substrate.

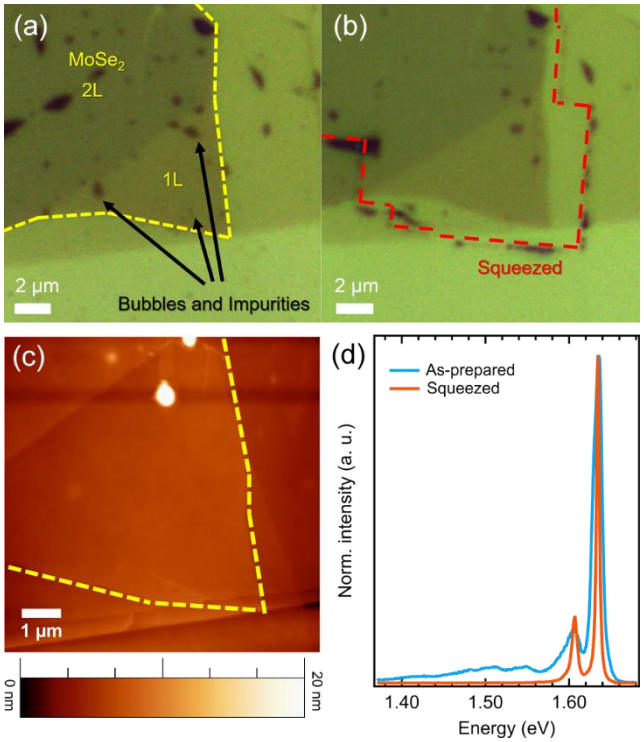

Figure 2 (a), (b) and (c) Optical microscope and AFM images of a hBN/$MoSe_2$/hBN sample before and after a squeezing process with applied force of 0.8 µN. Black dots in the optical images correspond to impurities/bubbles encapsulated between the $MoSe_2$ and hBN flakes. (d) Typical PL spectra of the sample before (blue) and after (orange) the squeezing process. Both spectra were measured at 10 K with excitation wavelength of 550 nm. After the squeezing process, reduction of linewidth and background are seen.

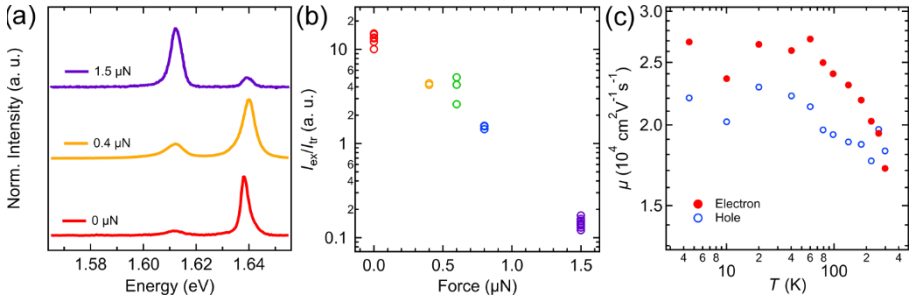

Figure 3 (a) PL spectra of hBN/$MoSe_2$/hBN samples measured at 10 K. Purple, orange and red curve correspond to spectra of samples squeezed at 0, 0.4 and 1.5 μN, respectively. Corresponding optical images of the samples are shown in Fig. S1. (b) Applied-force dependence of ratio of peak area of exciton and trion emission. (c) Temperature dependence of Hall mobility of electrons and holes in a hBN/graphene/hBN Hall bar. Saturation in Hall mobilities, which is caused by the charged impurity scatterings, are seen at low-temperature region.

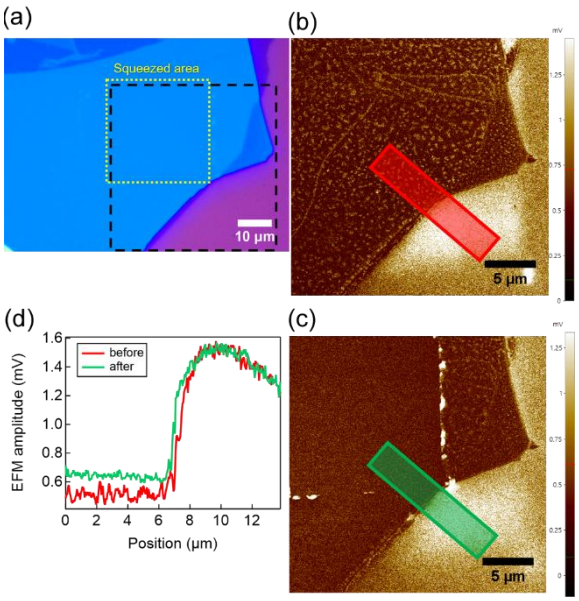

Figure 4 (a) An optical image of a hBN/hBN sample fabricated with the dry transfer method. A region surrounded by the yellow box is swept with applied force of 1.5 μN. (b) (c) EFM images before and after the squeezing process. (d) Line profiles of the EFM images along the long sides of red and green rectangles. The profiles are averaged using the regions surrounded by the rectangles. To cancel out possible shift arising from difference between AFM tips, EFM amplitude is shifted to make the EFM amplitudes at SiO_2 surface same.

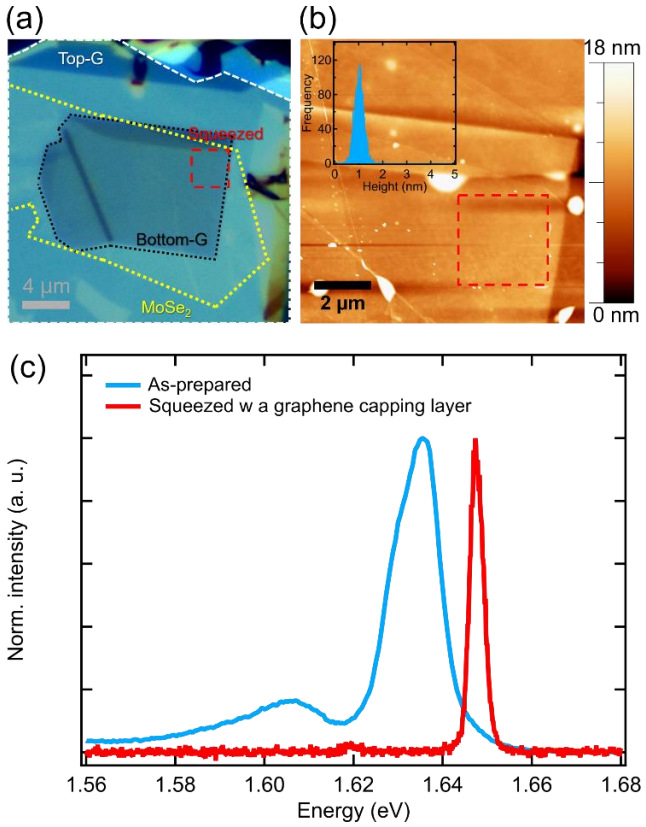

Figure 5 (a) An optical microscope image of a hBN/$MoSe_2$/hBN sample prepared with the GCAN method. Edges of the few-layer graphene capping layer and the bottom graphite are shown as white and black dotted lines, respectively. (b) An AFM image of the squeezed sample. The red dashed square shows the region squeezed with applied force of 1.5 μN. (inset) A height frequency distribution obtained at the squeezed region. RMS surface roughness reduces from 0.76 to 0.31 nm after the squeezing process. (c) PL spectra of hBN/$MoSe_2$/hBN samples, an as-prepared sample and the sample prepared with the GCAN method, measured at 10 K; excitation wavelength and photon flux are 633 nm and $\Phi ph \sim 2.3 \times 10^{19}$ $cm^{-2}s^{-1}$, respectively.

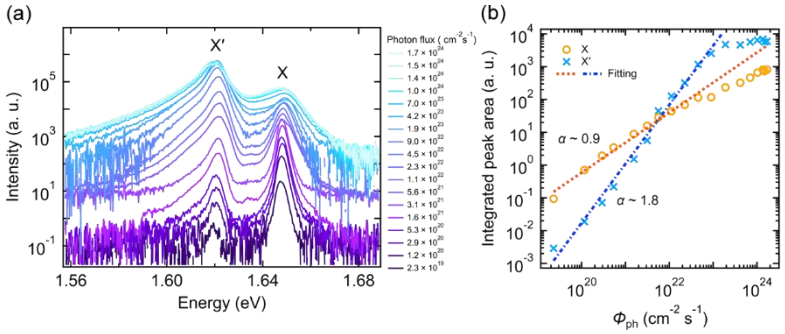

Figure 6 (a) Photon flux dependence of PL spectra measured at 10 K. The sample prepared with the GCAN method is excited at 633 nm HeNe CW laser. (b) log-log plots of integrated peak PL intensity *versus* photon flux, Φ_{ph}. Orange and blue points correspond to integrated peak intensity of exciton and trion emission, respectively. These plots can be fitted with exponent α of ~ 0.9 and ~ 1.8. Even in the smallest Φ_{ph}, generation of biexcitons is clearly seen.